

Machine Learning Analysis of Quasi-Stationary Magnetic Fields Optically-Driven by Short Laser Pulses

Iurii Kochetkov

Moscow Engineering Physics Institute

Nikolai Bukharskii

Moscow Engineering Physics Institute

Michael Ehret

University of Salamanca

Yuki Abe

Osaka University

Farley Law

University of Tokyo

Valeria Ospina

University of Salamanca

Joao Santos

Centre Lasers Intenses et Applications

Shinsuke Fujioka

Osaka University

Gabriel Schaumann

TU Darmstadt

Bernhard Zielbauer

TU Darmstadt

Andrey Kuznetsov

Moscow Engineering Physics Institute

Philipp Korneev (✉ korneev@theor.mephi.ru)

Moscow Engineering Physics Institute

Research Article

Keywords: Optical, Target-Normal Sheath Acceleration, radiochromic films

Posted Date: December 8th, 2021

DOI: <https://doi.org/10.21203/rs.3.rs-1129015/v1>

License: © ⓘ This work is licensed under a Creative Commons Attribution 4.0 International License.

[Read Full License](#)

Machine Learning Analysis of Quasi-Stationary Magnetic Fields Optically-Driven by Short Laser Pulses

I. V. Kochetkov¹, N. D. Bukharskii¹, M. Ehret², Y. Abe³, K. F. F. Law⁴,
V. Ospina-Bohorquez^{5,2,6}, J. J. Santos⁵, S. Fujioka³, G. Schaumann⁷, B. Zielbauer⁸,
A. Kuznetsov¹, and Ph. Korneev^{1,9,10,*}

¹National Research Nuclear University MEPhI, Moscow, Russian Federation

²Universidad de Salamanca, Salamanca, Spain

³Institute of Laser Engineering, Osaka University, Japan

⁴Graduate School of Science, The University of Tokyo, Japan

⁵Université de Bordeaux - CNRS - CEA, Centre Lasers Intenses et Applications (CELIA)
UMR 5107, Talence, France

⁶CEA, DAM, DIF, F-91297 Arpajon, France

⁷Institut für Kernphysik, Technische Universität Darmstadt, Germany

⁸PP/PHELIX, GSI, Darmstadt, Germany

⁹Lebedev Physical Institute, Moscow, Russian Federation

¹⁰Joint Institute for High Temperatures RAS, Moscow, Russian Federation

*korneev@theor.mephi.ru

December 2, 2021

Abstract

Optical generation of kilo-tesla scale magnetic fields enables prospective technologies and fundamental studies with unprecedentedly high magnetic field energy density. A question is the optimal configuration of proposed setups, where plenty of physical phenomena accompany the generation and complicate both theoretical studies and experimental realizations. Short laser drivers seem more suitable in many applications, though the process is tangled by an intrinsic transient nature. In this work, an artificial neural network is engaged for unravelling main features of the magnetic field excited with a picosecond laser pulse. The trained neural network acquires an ability to read the magnetic field values from experimental data, extremely facilitating interpretation of the experimental results. The conclusion is that the short sub-picosecond laser pulse may generate a quasi-stationary magnetic field structure living on a hundred picosecond time scale, when the induced current forms a closed circuit.

Conversion of laser light to magnetic field in laser-driven coils

Strong magnetic fields affect properties of matter on different scales [1]. In the Universe, they may reach the Schwinger limit ruling extremely energetic astrophysical processes, while being very modest though necessary for life on Earth. Magnetic fields of a certain strength for high-end laser-plasma applications are routinely produced in laboratories, either with high-voltage discharge drivers, or in an optical way, meaning that the electric currents are induced by intense laser pulses. Indeed, invention of the Chirped Pulse Amplification technique [2] potentiates laser radiation to possess an ultrahigh energy density and to become an excellent driver for strong electrical currents suitable for generation of extremely strong pulsed magnetic fields.

Several key approaches are extensively used for optical magnetic field generation (OMFG). The idea to use intense laser pulses for strong magnetic fields generation [3] followed observations of intense currents and spontaneous magnetic fields in experiments of laser interaction with matter. Since the first experiments with specifically designed targets [4] the optical approach is considered as a promising and convenient method. Generally, it is based on inducing electric currents in targets with certain loop-like geometries, when an intense

laser pulse interacts with another part of the target. These so called capacitor-coil targets with a mm-scale size work in a quasi-stationary regime [5, 6], the strong electron current forms a closed circuit exciting and sustaining a strong magnetic field near the target loop. A wide range of possible applications is foreseen for this scheme, e.g. controlling high-energy charged particles transport [7, 8], enhancing fusion output in experiments on laser-driven implosion of magnetized inertial confinement fusion targets [9, 10, 11] or producing magnetized plasma for laboratory studies of astrophysical processes [12, 13, 14]. Their compact size, no need of bulky and expensive capacitor banks and the ability to create magnetic fields one or two orders of magnitude higher than those reached with other methods make laser-driven generators preferable in many cases. Besides, various applications may require magnetic fields of different strength, geometry and temporal dependence, which may be effectively controlled by the parameters of laser pulses and the target.

Use of short laser pulses changes qualitatively the physics of magnetic field generation in capacitor-coil targets. The discharge may evolve rapidly and the setup needs optimization for efficient work. Intense short laser pulses are rather suitable for generation of energetic particles and secondary radiation, and they may also be more efficient for creating strong discharge electric currents, but just target size and setup down-scaling looks like an undesirable solution which limits many possible applications. Here, we show the way to reach a quasi-stationary operating regime in sub-millimeter targets with use of intense picosecond laser pulses.

When a short laser pulse interacts with an extended target, a short discharge pulse induced by the interaction propagates along the target [15] almost with the speed of light. To reach a quasi-stationary regime with short laser pulses, reduction of the target perimeter so it becomes less than the laser pulse length was proposed [16, 17, 18]. A reduced size of the coil in OMFG makes the effective magnetized volume quite small, so the principal question addressed here is whether the target with the coil perimeter longer than the pulse duration may produce a quasi-stationary magnetic field. In the presented experimental study, a coil-shaped target with a diameter $d \sim 100 \mu\text{m}$ is irradiated on the free end. For this size the time needed for a discharge pulse to close the circuit is $\approx \pi d/c \sim 1 \text{ ps}$, which appears to be longer than the 0.5 ps of the driver used. However, as shown below, if the circuit is closed before the discharge reaches the end of the coil, the generated magnetic field evolves towards stationary distribution. This allows to abstain from reducing the target size and shows the way of using powerful short laser pulses with practically interesting sub-millimeter targets.

The considered optically-driven magnetic field generator is a coil-shaped target, cut from $20 \mu\text{m}$ copper foil, shown in Fig. 1a & b. The laser beam is focused on the free end of the coil, as shown in Figs. 1 and 2. Under the irradiation, the hot electrons escape the target [19, 20] inducing a strong positive potential, which drives a discharge current along the target. As the laser pulse length is shorter than the coil perimeter, the discharge forms a finite pulse, which would go to the ground for an open circuit. However, as shown below, for a reasonable thin slit, plasma from the irradiated coil end fills it before the front of the discharge pulse comes. This closes the circuit and allows the current to form a self-consistent quasi-stationary structure with the magnetic field. The field was measured with proton radiography diagnostic [21, 22, 23]. In our study, the auxiliary protons generated with Target-Normal Sheath Acceleration (TNSA) mechanism [24] are passing through the magnetized region and deflecting there according to the local fields, leaving afterwards an imprint on the radiochromic films, see Fig. 1 and Supplementary Material for further insight. To ensure the presence of the magnetic fields for a long time after the irradiation, the probing time reached a few tens of picoseconds.

Experiment

Experimental study of optical magnetic field generation with coil-shaped targets was performed at the PHELIX laser facility at GSI in Darmstadt, Germany. Proton radiography was used as the main diagnostic for characterization of magnetic fields in the target region. The laser pulse with wavelength of 1056 nm and duration of 0.5 ps was divided into two beams - SP1 and SP2, each containing an energy of $\approx 50 \text{ J}$. The beams were tightly focused to a spot of $\approx 10 \mu\text{m}$ FWHM (full width at half maximum) using two parabolic mirrors with focal lengths of 400 mm (SP1) and 1500 mm (SP2), yielding relativistic intensities $\approx 10^{19} \text{ W/cm}^2$ on the targets. SP1 was focused on the open end of the coil target to excite strong discharge currents, while SP2 irradiated a thin gold foil, used as a source of diagnostic TNSA-accelerated protons [25], which then passed through the electromagnetic field near the coil target, see Fig. 2. An imprint of the fields, deviating the protons, was collected by a stack of several HD-V2 radiochromic films (RCF). The active layer of each RCF colorizes under exposure to ionizing radiation, producing a proton image that contains information about electromagnetic fields induced around the target. Multi-layer setup enables to characterize time evolution of the fields, since due to Bragg peak absorption of ions in matter each layer registers predominantly protons of one narrow energy range [26], passing the studied region at a certain moment of time. The coil target was probed at 27° to its axis, the distance between TNSA

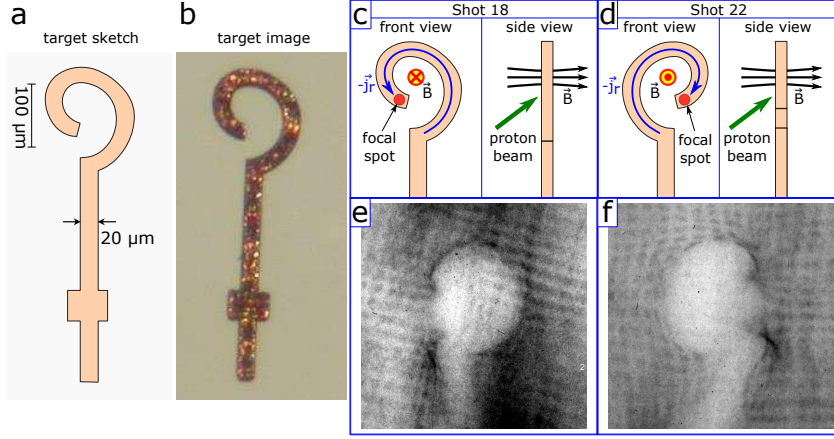


Figure 1: The target image (a) and its magnified image (b). Scheme of the setup used in Shot #18 (c) and #22 (d). Proton radiography image obtained in Shot #18 in the second layer of RCF stack, corresponding to Bragg peak position for ≈ 3 MeV protons, passing the studied region ≈ 25 ps after the end of the laser pulse; darker colors correspond to higher proton concentrations (e). The same for Shot #22 (f).

foil and the center of the coil target was 2.95 mm, the distance between the coil target center and the RCF plane was 163 mm, which corresponds to magnification factor of 56. Diagnostic protons had energies in the range of 1 – 6 MeV, yielding a time-of-flight difference of 130 ps for the specified distance between the target and proton source, and the time resolution of < 20 ps, if the signal on the second and subsequent layers of the RCF stack, corresponding to > 3 MeV protons, is considered. In order to distinguish diagnostic protons from protons emitted by the studied target, a metallic mesh with 1500 bars per inch was placed on the way of the probing proton beam.

Probing the generated fields in the experiment was performed for two opposing target orientations in shots #18 and #22, see Fig. 1 c & d and the obtained radiography images in Fig. 1 e & f. Their structure presents a void with distinct caustics on the boundary and a shadow of the target stalk. Analysis of the obtained radiographs is a non-trivial inverse problem. A viable and commonly used approach is to perform the data assessment by comparison of experimental radiographs with those obtained in synthetic ballistic simulations, where probe protons pass through model magnetic and electric fields. Parameters of the model fields are adjusted to match the radiographs. With some assumptions, it is possible [27] to estimate magnetic fields using only few geometric parameters of radiograph images. In general, deformation of the imprint from a rectangular mesh that is placed in the way of probe protons before they pass through the fields may be considered for analysis, though, for short laser pulses, it may be blurred because of the transient processes of the field formation, as it is in Fig. 1 c & d. Note that some geometric parameters of the radiograph may depend similarly on both magnetic and electric fields, both expected around the target, and analysis of the whole image is more robust as it may catch the entire structure formed by electromagnetic fields, rather than certain geometric features.

Neural Network application to experimental data analysis

Machine learning (ML) is the group of computer methods processing data with an algorithm, 'trained' in advance on completely characterized data sets. Nowadays, ML techniques are successfully employed in a broad range of research fields, including elementary particle physics and cosmology, quantum many-body physics, quantum computing, chemical and material physics [28]. ML can reduce computational costs and human workload in tasks involving large extensive data sets, e.g. the separation of pulsar signals from radio frequency interference [29]. ML methods can be used to make predictions without solving computationally costly equations for certain physical processes, e.g. dissolution kinetics of silicate glasses [30] and turbulence in subsonic flows [31]. Image processing is one of the most known ML applications. It is worth to note its use in image restoration in regular [32] and fluorescent microscopy [33], nonmodel-based bioluminescence tomography reconstruction [34], rapid decoding of the sample image from its hologram over an extended depth of field range [35], wavefront estimation [36] or robust photomask synthesis in inverse lithography technology [37]. Recently it has been demonstrated using synthetic data that ML in principle can be used to analyse proton radiography images and deduce important magnetic field parameters [38]. Here we develop this idea to reconstruct electromagnetic fields in real experimental setup

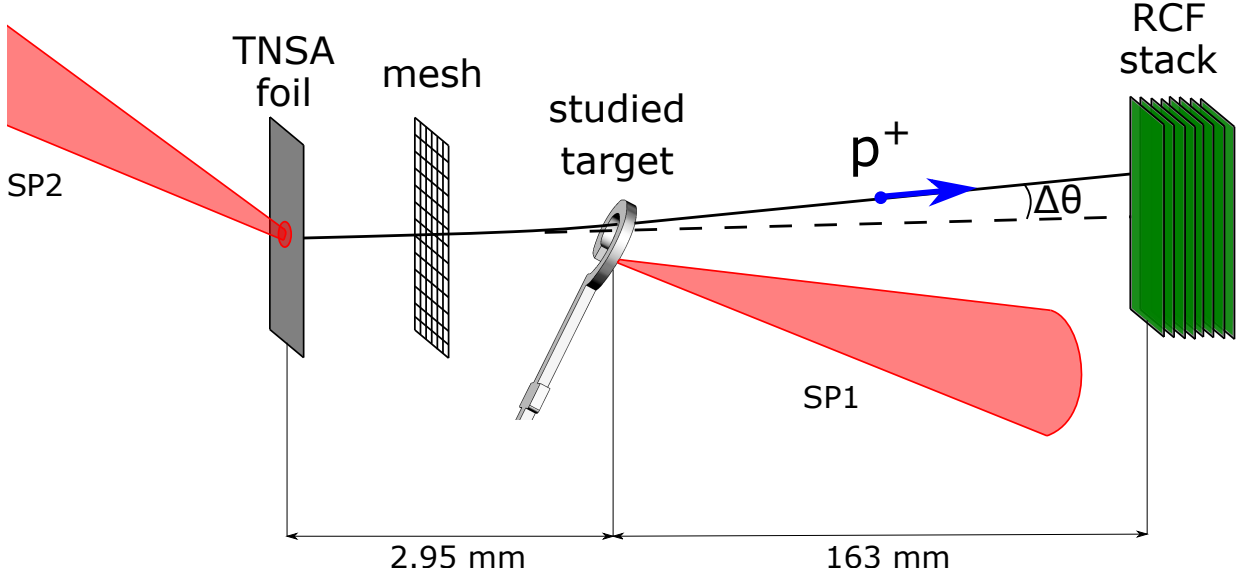


Figure 2: Sketch of the experimental setup for magnetic field generation and proton radiography measurements with two laser beams - SP1 and SP2.

using an Artificial Neural Networks (ANN), trained on numerically generated data.

In order to produce radiographs in ballistic simulations and to create synthetic data for the ANN training, model electromagnetic field distributions are required. For that, 2D Particle-in-Cell (PIC) calculations were performed using codes Smilei [39] and PICLS [40]. According to the results, detailed in the Supplementary Materials, the distribution of magnetic field in the target is mostly defined by surface electric currents. Therefore, the first key parameter to model magnetic fields is the current value \mathcal{J} along the target coil, closed through the expanded plasma near the irradiated coil end. Electric field distribution for ballistic simulations is defined by the target potential Φ , which is the second key parameter.

For analysis, a Convolutional Neural Network architecture was used, described in the Methods section, see Fig. 4a. It allows detecting similar 'informative' patterns in different parts of the data array [41] and thus enables extracting desired parameters for images where the main void structure may be shifted or tilted. It was found, that the main information about electromagnetic fields near the target is encrypted in geometry of the 'void' structure, which allowed to simplify the data and to reduce processing errors by using just the contour of the voids extracted from binarized images using OpenCV library tools. For training, 525 synthetic radiographic images with resolution of 300×300 were generated on a map (\mathcal{J}, Φ) with the total electric current $\mathcal{J} \in [2, 50]$ kA range with a step of 2 kA (the magnetic field in the coil center $\mathcal{B} \in [25.6, 640]$ T range with a step of 25.6 T) and the electric potential $\Phi \in [0, 100]$ kV range with a step of 5 kV. Using other parameters on this map, a set of 143 radiographs was created to validate the network. Additionally, slight random tilts and shifts were introduced to images from both datasets before they were loaded into the ANN. Parameters of the layers were adjusted to provide minimal training errors in a reasonable amount of training time, see the learning curves displaying the decrease of the mean squared error for training and validation data sets with the number of iteration (epoch) in Fig. 4b. Before loading the experimental data, the ANN with optimized kernels and weights underwent another verification with a completely new synthetic data set of 42 radiographs. After processing, the mean squared error for each key parameter was found to be less than a few percents.

The ANN was then applied for real experimental data imprinted in the second layer of RCF stack in Shot #18, processed as described above. The resulted current \mathcal{J} corresponds to the B-field of 282 T at the center of the coil and the target potential is $\Phi = 48$ kV. For these parameters, the synthetic radiograph is shown along with the experimental data in Fig. 4c. As even for a certain architecture ANN presents an intrinsic error, multiple trainings were performed to estimate the mean values of \mathcal{J}, Φ and their root-mean-square errors. After 21 training sessions these values were found as 265 ± 54 T for the magnetic field in the coil center and 47 ± 12 kV for the electric potential of the target.

The accuracy of the ML results was additionally studied with a correlation analysis. Two dimensional cross-correlation functions were calculated for the pairs of the experimental image and the synthetic images on the map

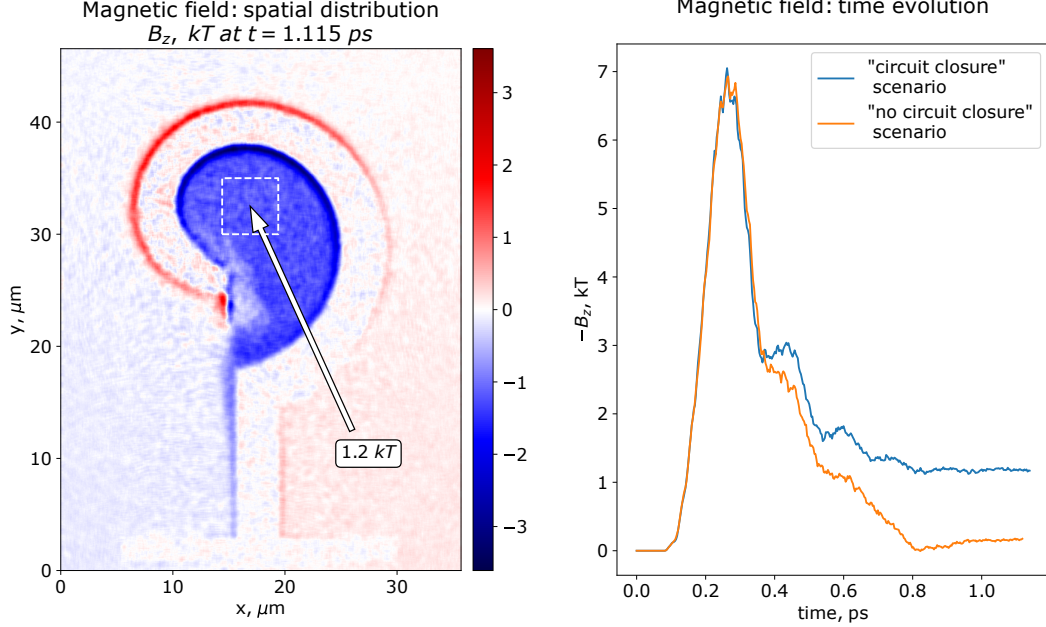


Figure 3: Results of 2D PIC simulations. Left panel: spatial distribution of magnetic field ≈ 0.75 ps after the end of the laser pulse, averaged spatially with a Gaussian kernel of $\approx 0.5 \mu\text{m}$ to reduce visual noise. Right panel: time evolution of the magnetic field inside the 'snail' cavity for two different scenarios of magnetic field generation; magnetic field is averaged over a $5 \times 5 \mu\text{m}^2$ square, marked with the white dashed line on the spatial distribution plot.

(\mathcal{J}, Φ) as $C(x, y) = \sum_{u,v} f(x, y)g(x+u, y+v)$, where f and g are the normalized pixel values of the experimental and synthetic images. The peak of the cross-correlation function was attributed to the image similarities. In Fig. 5 the distribution of the cross-correlation peak values are shown. The region of high correlation has the black cross in the center with error bars indicating deviation of the cross-correlation peak from its maximum for less than 0.01. From this consideration, the values of 257 ± 54 T are obtained for the magnetic field and $\Phi = 65 \pm 12$ kV for the electric potential. The CNN-based results are shown in the same plot by blue dots. They are scattered in the area shifted from the best-fit region in the correlation-based estimate. Average magnetic and electric field values are marked with the blue cross, with the error bars defined by the root-mean-square errors of 0.95 confidence level.

The observed deviation of the extracted parameters, obtained with two different methods, can be explained by the quality of the experimental image data as the errors appears to be reasonably small for the synthetic images. The observed systematic difference between the results obtained with the two different methods is related mostly to the potential Φ . So, it could be explained by the different treatment of a certain image feature related to the electric field. One such feature is the shadow of the target stalk, since the magnetic field in our consideration is mostly confined inside the target cavity. The size of the stalk shadow varies along the perimeter and it has no distinct borderline, see Fig. 4c. These irregularities may lead to a bias in the value of the extracted electric potential of the target observed.

A major advantage of the neural network-based method is its computational effectiveness in case of greater amount of experimental data. Initially, both methods used require a synthetic data set. With it, the neural network-based method requires a one-time computation of training the artificial neural network, while for the two-dimensional cross-correlation function calculation is necessary for each analysed image. Thus, neural network-based method is definitely preferable in case of an extensive parametric scan of a certain OMFG scheme.

Numerical Particle-In-Cell simulations

According to the numerical modelling, a quasi-stationary magnetic field is formed if the current circuit closes through the laser-generated plasma. An insight comes from the parametric scan, performed with the reduced

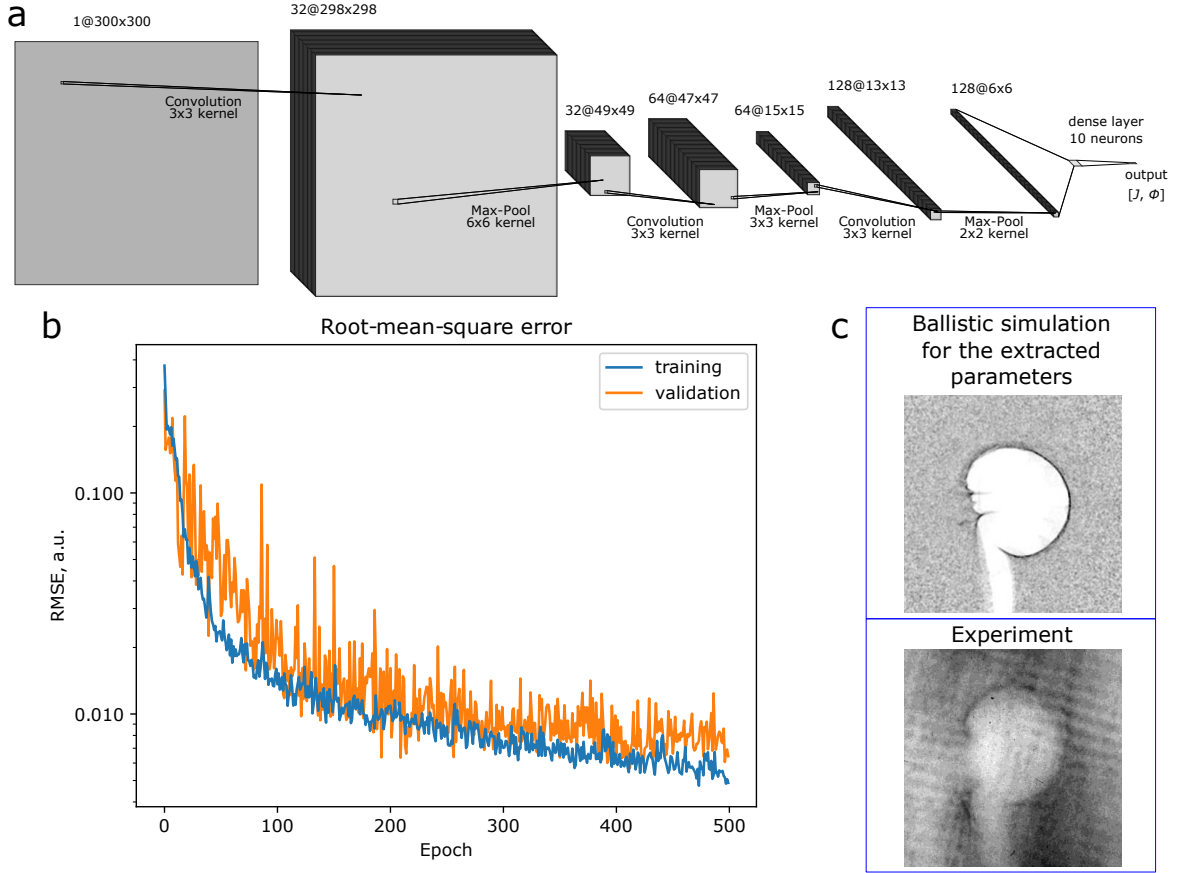


Figure 4: Architecture of the developed Convolutional Neural Network (a) and learning curves for training and validation data sets, displaying the decrease of the mean squared error with the number of epoch (b). Comparison of the synthetic proton image, obtained for the extracted parameters, with the experimental one for shot #18 (c).

simulation setup. Targets in this set of simulations consist of electrons (≈ 90 times the critical density) and ions with charge $Z = 10e$ and mass $A = 544$ corresponding to $\times 8.5$ the atomic mass of copper, to equate mass densities to the real values. The simulation box is $35.7 \mu\text{m} \times 46.5 \mu\text{m}$ or 5376×7008 cells with 10 particles of each kind per cell, the time step is $\approx 7.5 \cdot 10^{-3}$ fs. The laser intensity is $5.55 \times 10^{19} \text{ W/cm}^2$. Magnetic field distribution at ≈ 1.1 ps is shown in Figure 3 (left panel), it is almost uniform with an average value of ~ 1 kT. The temporal behavior of the magnetic field in the coil in this simulation is shown with a blue curve in Figure 3 (right panel). Following the fast growth up to ~ 7 kT at ≈ 0.25 ps, the magnetic field gradually decreases after the laser pulse ends. However, at ~ 0.8 ps the decrease stops at ~ 1 kT level. A quasi-stationary field distribution is formed and stays then for a time, much exceeding the laser pulse duration. This happens if the circuit closes through the gap between the end of the coil and its opposite side due to expansion of the laser-heated plasma with density high enough to sustain the current in the coil. For magnetic fields of ≈ 1 kT the surface current density is about $1 \text{ kA}/\mu\text{m}$. A simple estimate where the required electron density n_e in the gap is related to the surface current density j as $n_e = j/ewc$, where $w \approx 2 \mu\text{m}$ is the width of the conducting layer in the gap, and c is the speed of light, gives $n_e \sim 10^{19} \text{ cm}^{-3}$. In simulations, the electron density in the gap reaches $10^{18} - 10^{19} \text{ cm}^{-3}$, which is in a qualitative agreement with the obtained estimate. In contrast, if the circuit does not close before the laser-induced current pulse passes the coil, the magnetic field further decays to zero, as shown in Figure 3 (right panel), with an orange curve. This situation was modeled by increasing artificially the mass of ions by 36 times, which sufficiently decreases plasma expansion, so that the electron density in the gap does not exceed 10^{16} cm^{-3} when the discharge passes the coil length. In this case the discharge then propagates further to the stalk. The numerical analysis is presented in more details in the Supplementary Materials.

In the experiment, the magnetic field deduced from proton measurements corresponds to the total electric current of ≈ 20 kA. In order to evaluate electron density in the gap, estimate the number of electrons with the

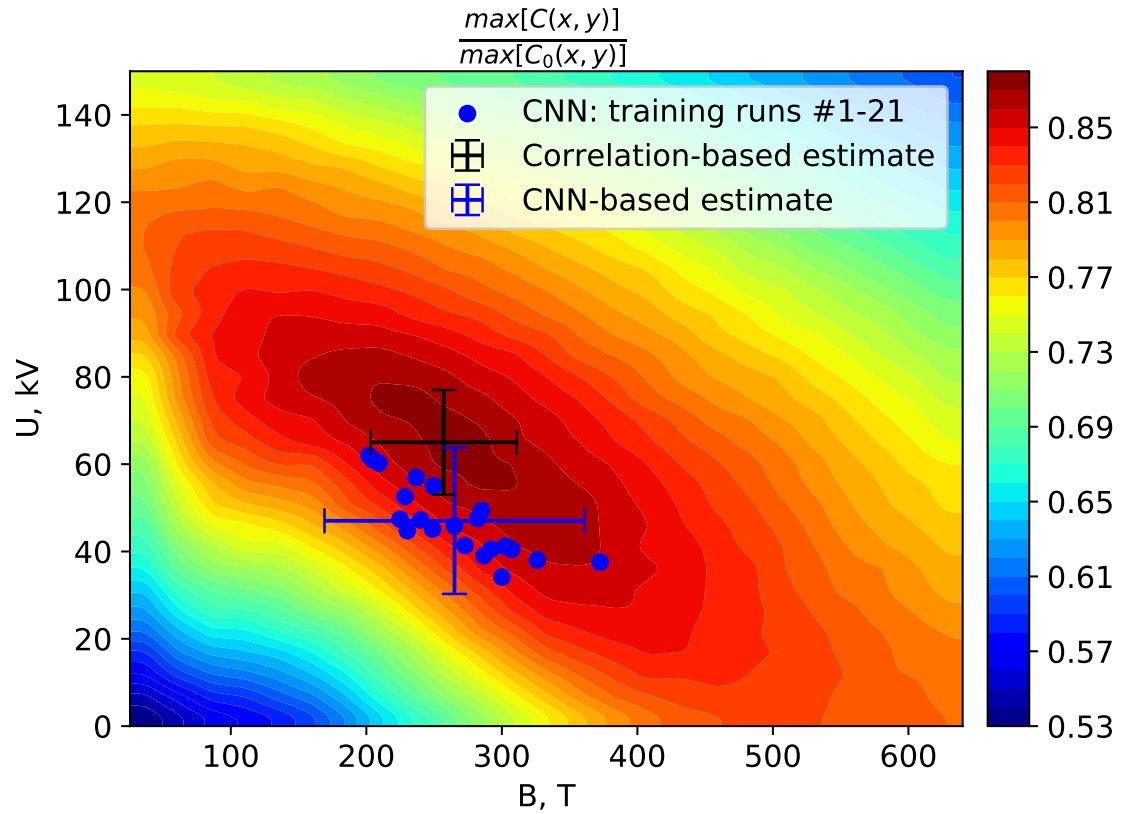


Figure 5: The peak value of cross-correlation between the normalised experimental and synthetic images as a function of the magnetic field in the target center and the electric potential of the target. The correlation peak values are normalized per maximum of the autocorrelation function $C_0(x, y)$. Black cross with error bars shows the best-fit for the region of the maximum cross-correlation peak value. Blue dots correspond to the values, obtained in each of the 21 ANN training runs, the blue cross and error bars correspond to the average magnetic and electric field values.

energy that obeys ponderomotive scaling $N_e = \chi E_{las} / (m_e c^2 \sqrt{(1 + \chi a_0^2/2)} - m_e c^2)$, where $\chi \sim 0.1..0.2$ is the laser absorption coefficient, $E_{las} = 50$ J is the total energy in the laser beam, $m_e c^2 \approx 0.5$ MeV is the electron rest energy and $a_0 \approx 3.8$ is the normalized vector potential that corresponds to the laser intensity of $2 \cdot 10^{19}$ W/cm². The result $N_e \approx 10^{15}$ is distributed in the volume of $\approx 50^3$ μm^3 , sufficient to close the internal tip of the spiral and its opposite end, the value of $\sim 10^{20}$ cm⁻³ is obtained for the average electron density in the gap. Multiplying it by a factor eSv , where $S = 10$ μm^2 is the area of a conducting layer and $v \approx c$ corresponds to the light velocity for relativistic electrons, we deduce the electric current ≈ 100 kA, which is enough to explain the stationary behavior of magnetic field observed in the experiment.

Outlook

Many foreseen optical-based applications, like particle acceleration, involve intense short laser pulses. For accelerated particle control, same laser pulses may create quasi-stationary electromagnetic structures, with a well controlled magnetic component, created by a closed current circuit in a coil. For potentially interesting big targets, the circuit closure may be controlled by the same laser driver, which excite the discharge current. With use of Neural Network, we deduce from the experimental data, obtained for several tens of Joules with a picosecond driver, that the magnetic field may reach a few hundreds of Tesla. The field structure remains stationary for tens of picoseconds due to the discharge circuit closure, which is evidenced by theoretical modelling. The presented machine-learning analysis shows a good accuracy and robustness though presence of a systematic error may depend on the data quality.

Acknowledgments

The results presented here are based on the experiment P171, which was performed at the PHELIX facility at the GSI Helmholtzzentrum für Schwerionenforschung, Darmstadt (Germany) in the frame of FAIR Phase-0. This research was carried out within the framework of the ‘‘Investments for the future’’ program IdEx Bordeaux LAPHIA (No. ANR-10-IDEX-03-02) and of the EUROfusion Consortium and has received funding from the Euratom research and training programs 2014–2018 under Grant Agreement No. 633053 (Enabling Research work programme 2017 CfP-AWP17-IFE-CEA-02). The views and opinions expressed herein do not necessarily reflect those of the European Commission. The work was partially supported by The Ministry of Science and Higher Education of the Russian Federation (Agreement with Joint Institute for High Temperatures RAS, No. 075-15-2020-785, dated 23 September 2020). This work was also granted access to the HPC resources of CINES under allocations Nos. A0020510052 and A0030506129 made by GENCI (Grand Equipment National de Calcul Intensif) and access to MEPhI HPC resources.

Methods

Synthetic data generation with ballistic proton simulations.

The training data was created in a set of ballistic simulations where Newton’s equations of motion for individual protons under the action of the Lorentz force were solved for different model magnetic and electric field distributions $d\vec{p}_i/dt = q_p \vec{E}(\vec{r}_i, \Phi) + q_p [\vec{V}_i \times \vec{B}(\vec{r}_i, \mathcal{J})]$, where \vec{r}_i , \vec{V}_i and \vec{p}_i describe the coordinates, velocity and momentum of a test proton with electric charge q_p at a time moment t , while $\vec{B}(\vec{r}_i, \mathcal{J})$ and $\vec{E}(\vec{r}_i, \Phi)$ are the quasi-stationary magnetic and electric fields at query points \vec{r}_i , proportional to the electric current in the loop \mathcal{J} and the electric potential of the target Φ , respectively. The magnetic field was calculated with 10 μm resolution using the Bio-Savart law under the assumption that it is formed by discharge currents flowing along the coil inner and outer surface. Electric field was calculated on the same 10 μm grid under the assumption that the target is charged to a certain potential. Protons in ballistic simulations were considered to originate from a point source. Charge-separation effects in the proton beam were neglected, as they are typically relatively low in TNSA-generated particle beams [42]. Thus, proton deflection was assumed to be caused purely by electromagnetic fields induced around the target. The force acting on a proton was linearly interpolated from the values at the grid points. Time resolution was chosen in accordance with the grid step Δ and initial proton velocity V_0 : $dt = \frac{\Delta}{2V_0}$. To account for a shadow produced in the beam by protons that hit the target material all particles with trajectories intersecting the target body were terminated from the simulation. Using such test particle approach, we created synthetic data sets for training, validating and testing the neural network for magnetic

field values at the target centre in the range from 25.6 T to 640 T and electric potential values in the range from 0 kV to 100 kV.

Neural Network architecture

For analysis of the obtained data, a Convolutional Neural Network architecture was used, as it allows detecting similar 'informative' patterns in different parts of the data array [41] and thus enables to extract desired parameters for images where the main proton void structure may be shifted. It is especially important when working with both synthetic and experimental data jointly, since it allows to skip an alignment of simulated to real image data. The first stage of our network consists of three convolutional layers, each followed by a pooling layer. The former are used to produce a set of feature maps by convolving the input image with different optimizable kernels. Each feature map, obtained with one specific kernel, is then transmitted through a nonlinear activation function, for which we used a common Rectified Linear Unit (ReLU): $f(x) = \max(0, x)$. The obtained data arrays undergo down-sampling in a pooling layer. This is achieved by dividing feature maps into small patches and taking local maxima as the new feature map 'pixel' values. Pooling effectively reduces the size of the data and the number of parameters for optimization, while substituting several neighboring 'pixels' with a single value makes ANN tolerant to small shifts and distortions in the analysed image. Output of the third pooling layer is flattened and sent to a fully-connected (dense) layer, connecting each node of the previous layer to every node of the subsequent final layer. It is composed of 10 neurons which take an input vector, apply to it optimizable weights and biases and pass it through an activation function. For this layer another common nonlinear function was used: $f(x) = \sigma(x) = (1 + e^{-x})^{-1}$. The described architecture is illustrated in Fig. 4a. The output layer has two nodes, corresponding to the two aforementioned key variables the ANN is trained to extract. The process of training implies iterative optimization of feature extracting kernels along with weights and biases of each neuron. On each iteration (epoch) loss function is calculated, which in our case presents mean squared error of extracting the two key parameters. Then the kernels and weights in every layer are updated to minimize the loss function. It is performed on the basis of an optimization algorithm, in this particular instance first-order gradient based optimization employing Adam algorithm [43] was used.

The learning curves displaying the decrease of the mean squared error for training and validation data sets with the number of iteration (epoch) are plotted in Figure 4b. Training took 500 epochs, until the loss function for the validation data set leveled out. Before loading the experimental data, the ANN with optimized kernels and weights underwent another verification - a completely new data set of 42 radiographs. After processing, the mean squared error for each key parameter was found to be 2 kA for the main current with typical values of ≈ 20 kA and 3 kV for the electric potential with typical values of several tens of kV. As the magnetic field is directly proportional to the current, its evaluation error is ≈ 26 T.

Cross-correlation analysis

Correlation analysis was employed as an additional method of retrieving electromagnetic field parameters. In order to implement it, we took the same data set that was used for the training of our neural network and complemented it with some additional data to characterize the degree of similarity in a broader range of electric potential values. For each image from this data set a two-dimensional cross-correlation function was determined by computing the sliding dot product of the experimental image with the given synthetic one. This enables finding similar features in both images regardless of their position in the image. Thus, when the main patterns corresponding to the 'void' structure overlap, the value of the cross-correlation function increases. The better the images overlap, the higher is their cross-correlation, making it a useful metric for determining the degree of similarity between two images. In our case, the maximum value of two dimensional cross-correlation was used. All the compared images were preprocessed - first, a mean pixel value was subtracted from each image and afterwards the image was divided by its standard deviation. This procedure enables to ensure that the increase of the cross-correlation peak is caused solely by the close overlap of the informative 'void' structures with each other and is unaffected by high background noise or different brightness of one of the two images. The resultant correlation peak values were divided by the value of the autocorrelation peak, which implies comparison of the experimental image with itself, thus making 1 the highest degree of similarity in such consideration, and interpolated on a grid with resolution 2.56 T for the magnetic field at the target centre and 0.5 kV for the electric potential of the target. As a result, two dimensional correlation maps with the distinct 'best-fit' region with high correlation in a certain range of parameters were obtained, enabling a simple estimation of the parameters of the fields and their comparison to the results, obtained with the artificial neural network.

A two dimensional plot in Fig. 5 shows the dependence of the value of cross-correlation peak on the magnetic field in the target center and the electric potential of the target. The correlation peak values are normalized per maximum of the autocorrelation function for which both f and g in the equation above are pixel values of the same experimental image. The region of high correlation and, hence, the region in which the field parameters provide the best fit to experimental data, has a prolonged oval shape, with the black cross in the center.

In the case of complex field distributions the described ANN approach would be much more computationally effective in a long run. After creating the synthetic data, the neural network-based method would require a one-time computational cost of training the artificial neural network, while for the other method computation of two-dimensional cross-correlation function would be necessary for each new analysed image. Thus, neural network-based method is more preferable when there are multiple images for the same target which need to be analysed. If the distribution of electromagnetic fields is the same for these images, and only its parameters are different due to, for example, different laser intensity or target material, it would only take a few seconds to preprocess the images and pass them through the trained network to obtain the values of these parameters. In order to illustrate this idea, we have estimated the total computational time which would be necessary with our computational resources to process 6 experimental images, corresponding to the same target, but, for instance, 3 different laser intensity levels and 2 different target materials, for the case when the electromagnetic field distribution is parametrized by 3 values instead of 2, as it was in this paper. The resultant total time is estimated to be about 28 hours with the neural network-based method and about 70 hours with the cross-correlation analysis. Although, despite obvious computational advantage of the former, it should be noted that its results lack in informativeness in comparison to the latter, since the correlation analysis allows to obtain a multi-dimensional map and estimate the size of the region where the parameters closely reproduce experimental ones, and thus properly estimate evaluation errors for these parameters. With a more complicated electromagnetic field structures, Machine Learning approach would allow to explain the data in a multi-dimensional parameter space, where other methods, like a cross-correlation analysis, would take too much time.

References

- [1] Dong Lai. “Matter in strong magnetic fields”. In: *Reviews of Modern Physics* 73.3 (2001), pp. 629–662. ISSN: 0034-6861. DOI: 10.1103/RevModPhys.73.629. arXiv: 0009333 [astro-ph]. URL: <http://link.aps.org/doi/10.1103/RevModPhys.73.629><http://journals.aps.org/rmp/abstract/10.1103/RevModPhys.73.629><http://journals.aps.org/rmp/pdf/10.1103/RevModPhys.73.629>.
- [2] Strickland D. and Mourou G. “Compression of amplified chirped optical pulses”. In: *Optics Communications* 56.3 (1985), pp. 219–221.
- [3] Korobkin V. V. and Motylev S. L. “Laser method for producing strong magnetic fields”. In: *Pisma v Zhurnal Tekhnicheskoi Fiziki* 5 (1979), pp. 1135–1140.
- [4] Daido H. et al. “Generation of a strong magnetic field by an intense CO₂ laser pulse”. In: *Phys. Rev. Lett.* 56.8 (1986), pp. 846–849.
- [5] J J Santos et al. “Laser-driven platform for generation and characterization of strong quasi-static magnetic fields”. In: *New Journal of Physics* 17.8 (Aug. 2015), p. 083051. ISSN: 1367-2630. DOI: 10.1088/1367-2630/17/8/083051. URL: <http://stacks.iop.org/1367-2630/17/i=8/a=083051?key=crossref.3c00c1af6faa070f173516ea5a628621><https://iopscience.iop.org/article/10.1088/1367-2630/17/8/083051>.
- [6] J. J. Santos et al. “Laser-driven strong magnetostatic fields with applications to charged beam transport and magnetized high energy-density physics”. In: *Physics of Plasmas* 25.5 (May 2018), pp. 1–11. ISSN: 10897674. DOI: 10.1063/1.5018735. arXiv: 1712.07175. URL: <http://arxiv.org/abs/1712.07175><http://aip.scitation.org/doi/10.1063/1.5018735><http://dx.doi.org/10.1063/1.5018735>.
- [7] Shohei Sakata et al. “Magnetized fast isochoric laser heating for efficient creation of ultra-high-energy-density states”. In: *Nature Communications* 9.1 (2018), p. 254101.
- [8] M. Bailly-Grandvaux et al. “Guiding of relativistic electron beams in dense matter by laser-driven magnetostatic fields”. In: *Nature Communications* 9.1 (Dec. 2018), p. 102. ISSN: 2041-1723. DOI: 10.1038/s41467-017-02641-7. arXiv: 1608.08101. URL: <http://arxiv.org/abs/1608.08101><http://www.nature.com/articles/s41467-017-02641-7>.

- [9] O. V. Gotchev et al. “Laser-Driven Magnetic-Flux Compression in High-Energy-Density Plasmas”. In: *Phys. Rev. Lett.* 103 (21 Nov. 2009), p. 215004. DOI: 10.1103/PhysRevLett.103.215004. URL: <https://link.aps.org/doi/10.1103/PhysRevLett.103.215004>.
- [10] P. Y. Chang et al. “Fusion Yield Enhancement in Magnetized Laser-Driven Implosions”. In: *Phys. Rev. Lett.* 107 (3 July 2011), p. 035006. DOI: 10.1103/PhysRevLett.107.035006. URL: <https://link.aps.org/doi/10.1103/PhysRevLett.107.035006>.
- [11] L. J. Perkins et al. “The potential of imposed magnetic fields for enhancing ignition probability and fusion energy yield in indirect-drive inertial confinement fusion”. In: *Physics of Plasmas* 24.6 (2017), p. 062708. DOI: 10.1063/1.4985150. eprint: <https://doi.org/10.1063/1.4985150>. URL: <https://doi.org/10.1063/1.4985150>.
- [12] X. X. Pei et al. “Magnetic reconnection driven by Gekko XII lasers with a Helmholtz capacitor-coil target”. In: *Physics of Plasmas* 23.3 (2016), p. 032125. DOI: 10.1063/1.4944928. eprint: <https://doi.org/10.1063/1.4944928>. URL: <https://doi.org/10.1063/1.4944928>.
- [13] Fei-Lu Wang et al. “Laboratory astrophysics with laser-driven strong magnetic fields in China”. In: *High Power Laser Science and Engineering* 4 (2016), e27. DOI: 10.1017/hpl.2016.27.
- [14] XU Shan-shan et al. “Numerical Simulation of Magnetic Reconnection Driven by the Laser Helmholtz Capacitor-coil Targets”. In: *Chinese Astronomy and Astrophysics* 45.2 (2021), pp. 131–146. ISSN: 0275-1062. DOI: <https://doi.org/10.1016/j.chinastron.2021.05.001>. URL: <https://www.sciencedirect.com/science/article/pii/S0275106221000229>.
- [15] K. Quinn et al. “Laser-Driven Ultrafast Field Propagation on Solid Surfaces”. In: *Physical Review Letters* 102.19 (May 2009), p. 194801. ISSN: 0031-9007. DOI: 10.1103/PhysRevLett.102.194801. URL: <https://journals.aps.org/prl/pdf/10.1103/PhysRevLett.102.194801> <https://link.aps.org/doi/10.1103/PhysRevLett.102.194801>.
- [16] Ehret M. et al. *Kilotesla plasmoid formation by a trapped relativistic laser beam*. 2019. eprint: [arXiv: 1908.11430](https://arxiv.org/abs/1908.11430).
- [17] K F F Law et al. “Relativistic magnetic reconnection in laser laboratory for testing an emission mechanism of hard-state black hole system”. In: *Physical Review E* 102.3 (Sept. 2020), p. 033202.
- [18] A. V. Brantov, Ph Korneev, and V. Yu Bychenkov. “Magnetic field generation from a coil-shaped foil by a laser-triggered hot-electron current”. In: *Laser Physics Letters* 16.6 (June 2019), p. 066006.
- [19] J.-L. Dubois et al. “Target charging in short-pulse-laser-plasma experiments”. In: *Phys. Rev. E* 89 (1 Jan. 2014), p. 013102. DOI: 10.1103/PhysRevE.89.013102. URL: <https://link.aps.org/doi/10.1103/PhysRevE.89.013102>.
- [20] A. Poyé et al. “Physics of giant electromagnetic pulse generation in short-pulse laser experiments”. In: *Phys. Rev. E* 91 (4 Apr. 2015), p. 043106. DOI: 10.1103/PhysRevE.91.043106. URL: <https://link.aps.org/doi/10.1103/PhysRevE.91.043106>.
- [21] P. Bradford et al. “Proton deflectometry of a capacitor coil target along two axes”. In: *High Power Laser Science and Engineering* 8.11 (2020), pp. 1–9. ISSN: 20523289. DOI: 10.1017/hpl.2020.9.
- [22] L. Willingale et al. “Proton deflectometry of a magnetic reconnection geometry”. In: *Physics of Plasmas* 17.4 (2010), pp. 1–5. ISSN: 1070664X. DOI: 10.1063/1.3377787.
- [23] Guoqian Liao et al. “Proton radiography of magnetic fields generated with an open-ended coil driven by high power laser pulses”. In: *Matter and Radiation at Extremes* 1.4 (July 2016), pp. 187–191. ISSN: 2468080X. DOI: 10.1016/j.mre.2016.06.003. URL: <http://linkinghub.elsevier.com/retrieve/pii/S2468080X16300310>.
- [24] M. Roth and M. Schollmeier. “Ion Acceleration - Target Normal Sheath Acceleration”. In: *CERN Yellow Reports* 1.November 2014 (2016), p. 231. DOI: 10.5170/CERN-2016-001.231. arXiv: 1705.10569. URL: <https://e-publishing.cern.ch/index.php/CYR/article/view/222> <http://arxiv.org/abs/1705.10569> <https://dx.doi.org/10.5170/CERN-2016-001.231>.
- [25] Roth. M. and Schollmeier M. *Ion Acceleration - Target Normal Sheath Acceleration*. 2016. eprint: [arXiv: 1705.10569](https://arxiv.org/abs/1705.10569).
- [26] Nürnberg F. et al. “Radiochromic film imaging spectroscopy of laser-accelerated proton beams”. In: *Review of Scientific Instruments* 80.3 (2009), p. 033301.

- [27] Santos J. J. et al. “Laser-driven strong magnetostatic fields with applications to charged beam transport and magnetized high energy-density physics”. In: *Physics of Plasmas* 25.5 (2018), p. 056705.
- [28] Carleo G. et al. “Machine learning and the physical sciences”. In: *Rev. Mod. Phys.* 91 (4 Dec. 2019), p. 045002.
- [29] Bethapudi S. and Desai S. “Separation of pulsar signals from noise using supervised machine learning algorithms”. In: *Astronomy and Computing* 23 (2018), pp. 15–26. ISSN: 2213-1337. DOI: <https://doi.org/10.1016/j.ascom.2018.02.002>.
- [30] Anoop Krishnan N. M. et al. “Predicting the dissolution kinetics of silicate glasses using machine learning”. In: *Journal of Non-Crystalline Solids* 487 (2018), pp. 37–45. ISSN: 0022-3093.
- [31] Zhu L. et al. “Machine learning methods for turbulence modeling in subsonic flows around airfoils”. In: *Physics of Fluids* 31.1 (2019), p. 015105. eprint: <https://doi.org/10.1063/1.5061693>.
- [32] Rivenson Y. et al. “Deep learning microscopy”. In: *Optica* 4.11 (Nov. 2017), pp. 1437–1443.
- [33] Weigert M. et al. “Content-aware image restoration: pushing the limits of fluorescence microscopy”. In: *Nature Methods* 15 (12 2018).
- [34] Gao Y. et al. “Nonmodel-based bioluminescence tomography using a machine-learning reconstruction strategy”. In: *Optica* 5.11 (Nov. 2018), pp. 1451–1454.
- [35] Wu Y. et al. “Extended depth-of-field in holographic imaging using deep-learning-based autofocusing and phase recovery”. In: *Optica* 5.6 (June 2018), pp. 704–710.
- [36] Paine S. W. and Fienup J. R. “Machine learning for improved image-based wavefront sensing”. In: *Opt. Lett.* 43.6 (Mar. 2018), pp. 1235–1238.
- [37] Jia N. and Lam E. Y. “Machine learning for inverse lithography: using stochastic gradient descent for robust photomask synthesis”. In: *Journal of Optics* 12.4 (Mar. 2010), p. 045601.
- [38] Chen N. F. Y. et al. “Machine learning applied to proton radiography of high-energy-density plasmas”. In: *Phys. Rev. E* 95 (4 2017), p. 043305. DOI: 10.1103/PhysRevE.95.043305.
- [39] Derouillat J. et al. “Smilei: A collaborative, open-source, multi-purpose particle-in-cell code for plasma simulation”. In: *Computer Physics Communications* 222 (2018), pp. 351–373.
- [40] Y. Sentoku and A.J. J. Kemp. “Numerical methods for particle simulations at extreme densities and temperatures: Weighted particles, relativistic collisions and reduced currents”. In: *Journal of Computational Physics* 227.14 (July 2008), pp. 6846–6861.
- [41] LeCun Y., Bengio Y., and Hinton G. “Deep learning”. In: *Nature* 521 (7553 2015), pp. 436–444.
- [42] T. E. Cowan et al. “Ultralow Emittance, Multi-MeV Proton Beams from a Laser Virtual-Cathode Plasma Accelerator”. In: *Phys. Rev. Lett.* 92 (20 May 2004), p. 204801. DOI: 10.1103/PhysRevLett.92.204801. URL: <https://link.aps.org/doi/10.1103/PhysRevLett.92.204801>.
- [43] Kingma D. P. and Ba J. *Adam: A Method for Stochastic Optimization*. 2014. eprint: 1412.6980.

Author contribution statement: IVK, NDB, ME, YA, KFFL, VOB, JJS, BZ prepared and performed the experiment, NDB, SF, AK, PhK analyzed the results, GS prepared targets, NDB and PhK wrote the main text.

Supplementary Files

This is a list of supplementary files associated with this preprint. Click to download.

- [NeuralNetworkpaperSupplement.pdf](#)